



## Equation of state measurements of dense krypton up to the insulator-metal transition regime: Evaluating the exchange-correlation functionals

Zhao-Qi Wang <sup>1,2</sup> Yun-Jun Gu,<sup>1</sup> Qi-Feng Chen <sup>1,\*</sup> Zhi-Guo Li,<sup>1</sup> Lei Liu,<sup>1</sup> Guo-Jun Li <sup>1,2</sup>  
Yang-Shun Lan,<sup>1,2</sup> and Xiang-Rong Chen<sup>2,†</sup>

<sup>1</sup>National Key Laboratory for Shock Wave and Detonation Physics Research, Institute of Fluid Physics, Chinese Academy of Engineering Physics, Mianyang 621900, People's Republic of China

<sup>2</sup>College of Physics, Sichuan University, Chengdu 610065, People's Republic of China



(Received 6 November 2020; accepted 5 January 2021; published 14 January 2021)

Motivated by the poor understanding of the applicability of new exchange-correlation (XC) functionals to warm dense matter (WDM), we designed and performed multiple-shock reverberation compression experiments on dense krypton to evaluate explicitly the implications of recently derived XC functionals. The equation of states of krypton up to 155 GPa and 45 000 K, which ranges from an initial dense gaseous state up to the insulator-metal transition regime, were determined accurately. It is found that the experimental data are better reproduced by the strongly constrained and appropriately normed (SCAN) XC functional compared to the conventional Perdew-Burke-Ernzerhof and Van der Waals (vdW) DF1 functionals, elucidating that the introduction of the kinetic energy density and the intermediate-range vdW interaction is decisive. However, the incorporation of long-range interactions into the SCAN (SCAN + rVV10 XC functional) results in a noticeably stiffer prediction due to an overestimation of the density and internal energy of the system at low densities and temperatures. Our evaluation of the Karasiev-Sjostrom-Dufty-Trickey free-energy functional experimentally validates the XC thermal effect in the WDM regime, verifies the previous predictions, and sheds light on a direction for future theoretical efforts. Finally, a phase diagram of krypton is given, which provides a clear picture for understanding the thermophysical behavior of krypton in a wider temperature-pressure range.

DOI: [10.1103/PhysRevB.103.014109](https://doi.org/10.1103/PhysRevB.103.014109)

### I. INTRODUCTION

Understanding how matter behaves under extreme conditions, such as in a warm or hot dense state, is the purview of high-energy-density physics, inertial confinement fusion [1], planetary science [2,3], and laboratory astrophysics [4]. Under such dense conditions, noble gases (NGs) are often used as a model system to explore the processes above due to their chemical inertness and importance in the astrophysics [3,5,6]. Of all the NGs, the high-temperature ( $T$ ) and pressure ( $P$ ) responses of helium, neon, argon, and xenon have been measured extensively [7–12], whereas that of krypton has received relatively less attention. Moreover, most diamond-anvil cell experiments on solid krypton have been focused on confirming the martensitic transformation [13–15] and determining the equation of state (EOS) at room temperature [13,15–19] and the melting line [5,20], without considering the impact of the high  $T$ - $P$  conditions on its thermophysical behavior. Experimental realizations of liquid krypton are also incomplete, and there is a pressure gap between previous high-explosive shock experiments ( $P < 90$  GPa) [21] and recent  $Z$  machine experiments ( $P > 344$  GPa) [22]. Actually, krypton is a decay product of nuclear fission [23] and a unique geochemical tracer of the origins of the degassing history

of the mantle [3,5,24], describing the thermophysical behavior of krypton accurately in the warm dense matter (WDM) region is essential for modeling the processes in a nuclear reactor and for resolving the structure and dynamics of the planet.

Theoretically, *ab initio* molecular dynamics (AIMD) is an efficient approach for predicting and elucidating the thermophysical behavior of condensed materials [25–27], but in practice approximations must be adopted to describe many effects. These approximations included in the exchange-correlation (XC) functional, are exact for the ground-state calculation, but sometimes will encounter difficulties in describing the WDM. A prominent example is that the Perdew-Burke-Ernzerhof (PBE) and other XC functionals struggle to describe well the compression behavior of neon [12] and argon [28] in the WDM regime and give stiffer results. Reliable prediction requires accurate XC functional adequate to the WDM conditions. Recent advances in density functional theory (DFT), including the strongly constrained and appropriately normed (SCAN) metageneralized-gradient approximation functional [29,30], and the Karasiev-Sjostrom-Dufty-Trickey (KSDT) finite-temperature free-energy functional [31–33], make the incorporation of the van der Waals (vdW) interactions and the XC thermal effects feasible. Although these XC functionals can achieve remarkable accuracy when describing the thermophysical behavior of some materials compared to the PBE functional, their applicability to heavier elements in the WDM regime remains to be explored and verified.

\* chenqf01@gmail.com

† xrchen@scu.edu.cn

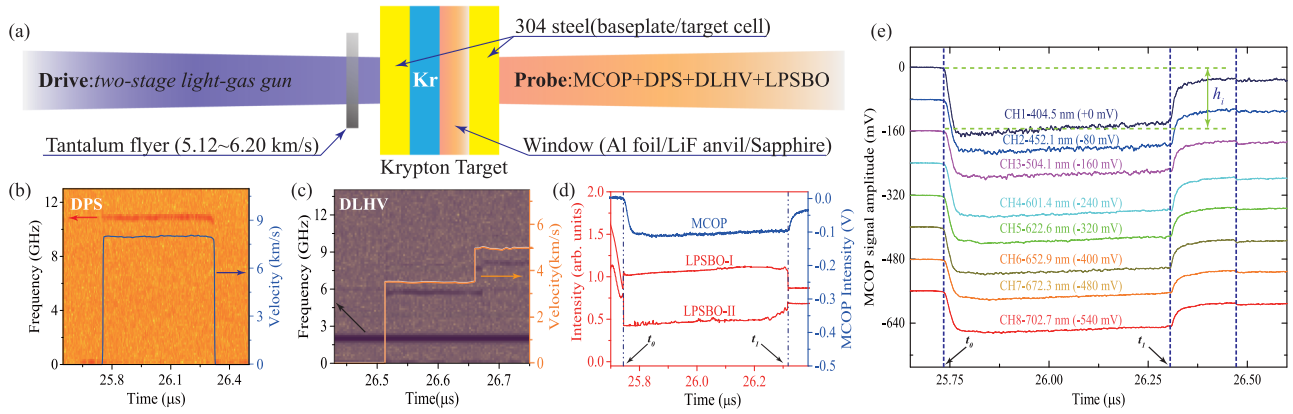


FIG. 1. Experimental concept (not to scale). (a) Sketch of the experimental target used to obtain the multishock states of dense krypton. (b) The velocity history of the shock front monitored by the DPS. (c) The velocity profiles of sample/LiF interfaces measured by the DLHV. (d) The cross-check of the first-shock transmit time recorded by the MCOP and LPSBO system. (e) The time-resolved self-emission of the shocked krypton measured by MCOP at wavelength ranging from 404.5 nm, and the voltage signal amplitude ( $h_i$ ) shifting to these numbers in parentheses. The other detailed description and the arrangement of diagnostic probes can be seen in the SM [34].

The dynamic compression of materials through shock wave experiments has been paramount in guiding our understanding of the high  $T$ - $P$  responses of materials and in evaluating the emerging computational techniques, such as AIMD techniques [12,25,27,33,35,36] and various chemical models [37,38]. Therefore, in this paper, we design and perform a series of shock experiments on dense krypton using a shock reverberation technique, and present the experimental EOSs of dynamically compressed dense krypton in the WDM regime. The achievable wide-range EOS, which ranges from an initial dense gas up to the insulator-metal transition regime, not only bridges the pressure gap between high-explosive shock experiments and the  $Z$  machine experiments, but also provides a useful assessment for new XC functionals and other existing models.

## II. EXPERIMENTAL METHODS

Our experimental system builds on advanced multiple-shock reverberation compression experiments to generate much-longer time scales and much-larger sizes of WDM, thereby allowing high-precision EOS measurements [12,39]. Figure 1(a) and Figs. S1-S5 in the Supplemental Material (SM) [34] are sketches of the experimental target and analysis of the shock compression processes. All the design parameters of experimental target have been simulated and checked by our one-dimensional hydrodynamic code (see Fig. S4 [34]). Before shock compression, the dense gaseous krypton was enclosed within the sandwich structure between two high shock impedance materials including a 304 steel baseplate and a composite window, and it was precompressed up to  $\sim 40$  MPa at room temperature. The composite window consisted of a  $\sim 0.13$ -mm-thick aluminum (Al) reflecting foil, a  $\sim 4.0$ -mm-thick lithium fluoride (LiF) anvil, and a  $\sim 2.0$ -mm-thick sapphire sheet, and it was used to monitor the shock wave transit time and the shock-induced spectral radiation for the compressed sample. The tantalum flyer, with a dimension of  $\sim 28$  mm in diameter and  $\sim 3.2$  mm in thickness, was accelerated by a two-stage light-gas gun with a bore diameter of  $\sim 30$  mm up to  $5.12 \sim 6.20$  km/s, which

was measured via a magnetic velocity induction system with uncertainties about 0.5%. Then the strong planar shock waves were generated when the tantalum flyer impacted on the front surface of the baseplate at high velocity. Once the shock wave transmitted into the sample across the baseplate, the multiple-shock reverberation compression will be achieved between the baseplate and the composite window due to their higher shock impedance than that of the sample. During the repeated propagation and reverberation of the shock wave, the thermophysical parameters of dense krypton, including densities ( $\rho$ ),  $T$ , and  $P$ , gradually increased, and finally the sample entered into the WDM regime.

The relevant signal collection systems are as follows. The Doppler pins system (DPS) and dual laser heterodyne velocimetry (DLHV) system with an operating wavelength of 1550 nm were designed to measure the velocity profiles of the shock front and sample/LiF interfaces, respectively, as displayed in Figs. 1(b) and 1(c). The laser photomultiplier shock breakout (LPSBO) system was selected to record the first-shock transmit time with higher accuracy because the jump time of light reflection signals ( $\sim 1$  ns) monitored by it is smaller than that of multichannel optical pyrometer (MCOP). The cross-check of the first-shock transmit time measured by the MCOP and LPSBO systems is shown in Fig. 1(d). The MCOP, carefully calibrated through a standard bromine-tungsten lamp, was used to record the spectral radiance history of the shocked krypton within a wavelength ranging from 404.5 to 702.7 nm. The flat region of the MCOP between  $t_0$  and  $t_1$  [see Fig. 1(e)] indicates that the shock wave transmitted across the sample with good uniformity. The refractive index of the unshocked samples and the thickness of the sample chamber under pre-compression condition were measured accurately by our-designed optical-fiber frequency domain interferometer device [40]. For each shot, the shock states of krypton were determined using the Monte Carlo impedance matching [41–44]. This approach ensures the propagation of all random measurement errors and systematic errors in the baseplate and composite window [35,45–47]. Further details of the experimental target, representative signals, refractive index [40], Rankine-Hugoniot relations, uncertainty analysis,

experimental data, and computational method [48–50] can be found in the SM [34].

### III. RESULTS AND DISCUSSIONS

In our experiments, a total of four measurements of dense krypton were performed over the density, temperature, and pressure ranging from 0.206 to 6.62 g/cm<sup>3</sup>, 300 to 45 000 K, and 5.44 MPa to 155 GPa, respectively, as illustrated in Tables S3 and S4 [34]. The principal- and off-Hugoniot of krypton were successfully obtained from each shot, and a higher compression ratio ( $\sim 28$ -fold; Fig. S11 [34]) was achieved. These data cover a wide  $\rho$ - $P$  regime and provide a good platform for discriminating the subtle differences between DFT models, especially for the new DFT XC functionals. Therefore, we employed the PBE [51], vdW-DF1 [52], SCAN [29], and the SCAN in combination with the revised Vydrov-Van Voorhis (SCAN + rVV10 [53]) functionals to describe the high  $T$ - $P$  response of the dense krypton. Calculations were performed with the VASP code [54]. We also compared the results with those for the KSDT [31] free-energy functional (implemented via the Profess@Quantum-Espresso interface [55,56]) and for the existing EOS models (self-consistent fluid variational theory (SFVT) [37] and SESAME [38]). Results for shots GKr180604 and GKr180605 which had the same initial states except for the flyer's velocity ( $V_f$ ), and the shot GKr180705 which had a higher initial density, are displayed in Fig. 2. The results of other shots are shown in Figs. S10 and S12 [34]. The shot-to-shot reproducibility of our dynamic experiments was confirmed well by shots GKr180604 and GKr180605, as illustrated in Fig. 2(a) and Fig. S9 [34]. Note that the subsequent shock states predicted by the different models depend on the initial state of the dense krypton and on the impedance-matching method, which can significantly magnify the differences in the observable quantities.

The various XC functionals were evaluated quantitatively by comparing the fitting between the DFT and experimental results. For the AIMD results, as shown in Fig. 2 and its insets, the PBE, vdW-DF1, and SCAN functionals can reliably reproduce the experimental  $\rho$ - $P$  data within the uncertainties up to 155 GPa. Moreover, the predictions by the SCAN, especially for shot GKr180705, as displayed in Fig. 2(b), are slightly softer than those of PBE and vdW-DF1, showing considerable improvement of its predictive capability for EOS over a wide  $\rho$ - $P$  region. This elucidates that including contributions of both the kinetic energy density and the intermediate-range vdW to the internal energy of dense krypton is more important than previously recognized. However, the results for SCAN + rVV10 differ noticeably from the experimental data and other DFT predictions. It appears that the treatment of the long-range vdW interactions by incorporating rVV10 into SCAN does not lead to any performance improvement for dense krypton. Therefore, we examined further the internal energy, pressure, and pair correlation function (PCF) of the initial states of krypton using these functionals. As seen in Table. S2 [34], the PBE, vdW-DF1, and SCAN functionals yield positive pressures and larger positions of the first peak of the PCF. However, the SCAN + rVV10 simulation yields negative pressures and smaller positions of the first peak of the PCF, indicating that the interactions are excessively

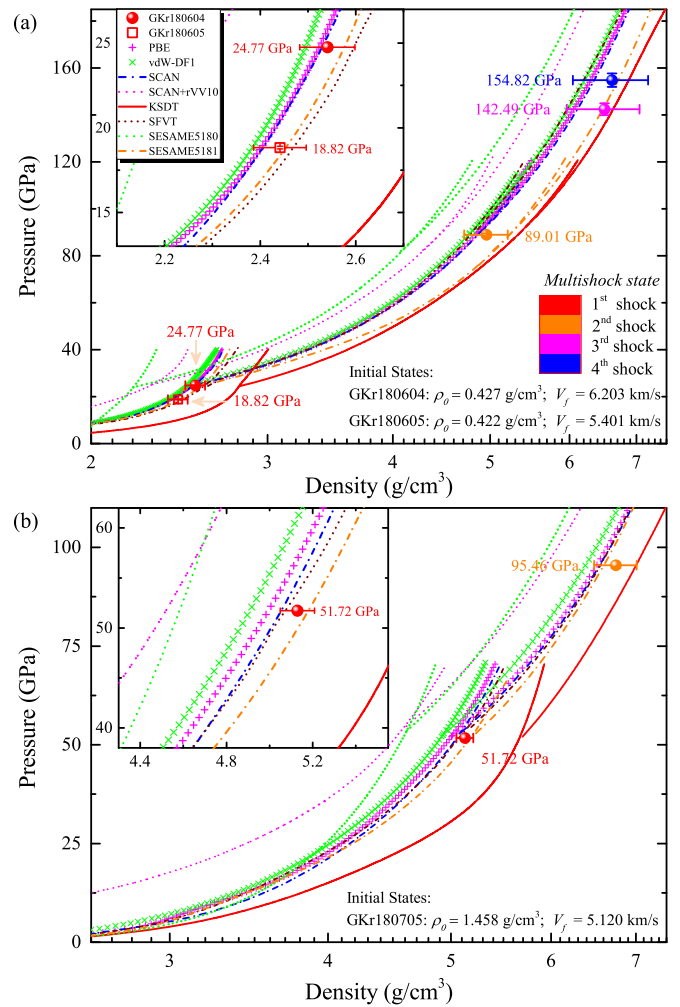


FIG. 2. The measured shock experimental  $\rho$ - $P$  data for shots (a) GKr180604 and GKr180605, and (b) GKr180705 [for which the legend is the same as that in (a)]. The insets show the first-shock state (principal Hugoniot) of dense krypton. Our experimental data (solid ball and square) were compared with AIMD calculations obtained by using five different XC functionals (PBE [51], vdW-DF1 [52], SCAN [29], SCAN + rVV10 [53], and KSDT [31]) and the existing EOS models (SFVT [37], SESAME 5180, and SESAME 5181 [38]). Error bars represent standard deviations at the  $1\sigma$  level and include random and systematic uncertainties.

attractive under low  $\rho$ - $T$  conditions. This inconsistency is also evidenced in the liquid water [36], where the overstructured PCF and negative pressure obtained by the SCAN + rVV10 calculation lead to a significant overestimation of the density and internal energy of the system. This insight into the shortcomings of the latter should aid in future theoretical efforts.

For the KSDT functional, we can clearly see that the  $\rho$ - $P$  data calculated by this functional is lower than those of ground-state functionals. The results deviate significantly from the lower shock states, especially for lower densities and temperatures. This is because this functional is derived via a thermodynamic analysis of restricted-path-integral Monte Carlo data with the Wigner-Seitz radius  $r_s = (3/4\pi n)^{1/3} a_0^{-1}$  ranging from 1.0 to 40 and the reduced temperature  $\theta = T/T_F$  ranging from 0.0625 to 8.0 [57], which is far below our

experimental initial state of gaseous krypton with  $\theta \gg 8$ . With the elevation of temperature, our experimental states approach to the regime mentioned above, thereby the deviation decreases and the predictions yield an improved agreement with the higher shock state. This implies that the inclusion of the XC thermal effects may provide a better description of our experimental results at high temperatures. Note that the present comparisons between the experimental data and the AIMD simulation for krypton are a narrow test of these functionals. The applicability of these functionals in a wider regime may need to be confirmed by more comparisons between the theoretical simulations and the experimental data for different kinds of materials under various conditions. For other existing EOS models, the results from SFVT and SESAME 5181 models are consistent with the experimental data, especially for the SFVT. Its accuracy is comparable to that of the DFT calculations considered here. However, SESAME 5180 obviously overestimates the pressure and gives stiffer results deviating from the experimental data. This may be due to the high  $P$ - $T$  nature of the ionization and the high-temperature radiation effect, which have been taken into account in our SFVT model. The difference between SESAME 5180 and SESAME 5181 is possibly related to the different treatments of the electronic contributions in the Helmholtz free energy [22].

Temperature is fundamental to thermodynamics and is an important constraint to benchmark EOS models, but  $T$  is no part of the Rankine-Hugoniot relation typically and must be measured separately from shock  $\rho$  and  $P$ . Here, we used a set of MCOP to record the time-resolved spectral radiance histories of the shocked samples [see Fig. 1(e)]. Then, the shock temperature  $T$  was extracted by fitting the absolute spectral radiance to a gray-body Planck spectrum multiplied by the emissivity,  $\epsilon(\lambda)$ , which was estimated from the reflectivity of the shock front within the Smith-Drude model [58]. The applicability of this model in the WDM regime has been confirmed for the liquid krypton (Fig. S7 [34]) and other liquid materials, such as hydrogen [59], argon [11], mercury, and tellurium [58]. The experimental spectral radiance and the Planck radiation fitting are shown in Fig. S8 [34], and the obtained first-shock temperatures are listed in Table S5 [34]. Note that the second- to fourth-shock temperatures could not be obtained in our experiments because the LiF was ablated by the shock-generated high temperatures at the krypton/LiF interface [see Fig. 1(e)]. Therefore, the research of the high- $T$  resistant materials capable of recording the optical radiation for the shock states remains an ongoing challenge. Figure 3 shows the experimental data and the results for different theoretical models of the first-shock temperature. As can be seen, the PBE, vdW-DF1, SCAN, SFVT, and SESAME 5181 results agree reasonably with the experiments, whereas the KSDT, SCAN + rVV10, and SESAME 5180 deviate significantly from the experiments, which are consistent with the previous  $\rho$ - $P$  comparisons. The insight gained from these high  $T$ - $P$  measurements and calculations may provide an effective way to discriminate the present XC functionals and to evaluate future theoretical developments.

Considering the importance of krypton in astrophysics [61] and geophysics [5,24], our experimental data and those from

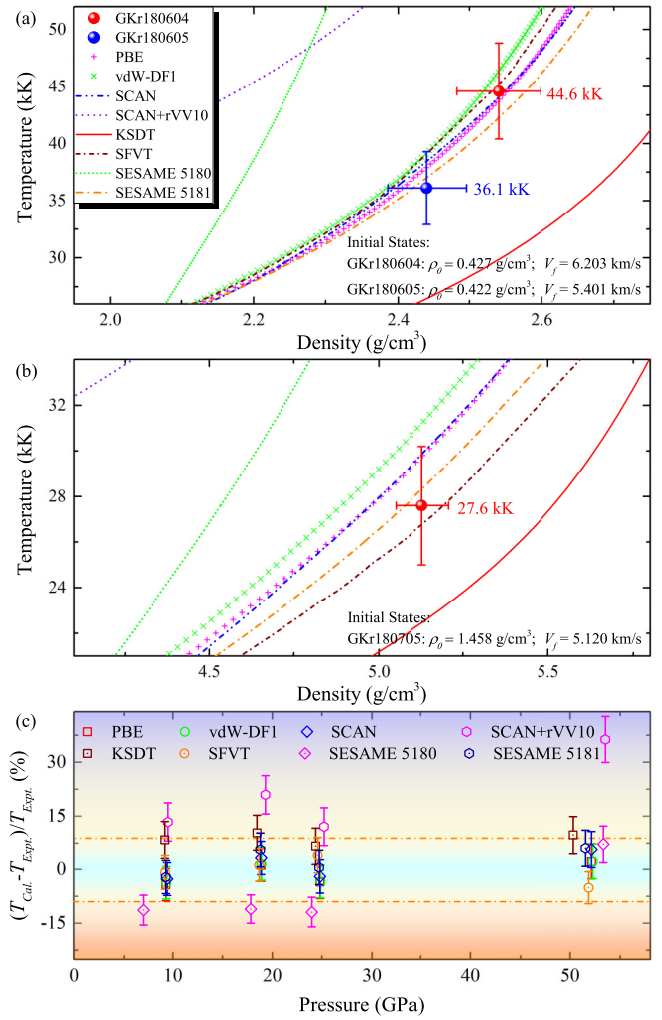


FIG. 3. The measured first-shock temperatures. Comparisons between the experimental data and different theoretical results for shots: (a) GKr180604 and GKr180605, and (b) GKr180705 [for which the legend is the same as that in (a)]. (c) Relative differences between the experimental data and the theoretical results for four shots. The experimental uncertainties at the  $1\sigma$  level are shown as the central bright color region around 0. The experimental temperatures were extracted from MCOP signals using the Smith-Drude model [58] and the gray-body Planck function.

Refs. [5,20,21] make it possible to obtain the high  $T$ - $P$  phase diagram of krypton to understand its thermophysical behavior in a wider regime of physical environments, as shown in Fig. 4. Accordingly, the compression states of dense krypton are characterized by the coupling parameter and optical conductivity, which were estimated using the SFVT model and DFT calculations, respectively. The resultant coupling parameter  $\Gamma = \frac{(Ze)^2}{k_B T} \left(\frac{4\pi}{3} n\right)^{1/3}$  ranges from 1.0 to 3.4, and the degeneracy parameter  $\Theta = \frac{2m_e k_B T}{\hbar} (3\pi^3 n_e)^{-2/3}$  ranges from 1.2 to 4.9, attesting that the shock states of krypton are mostly degenerate, strongly coupled, and nonideal, thereby they enter into the WDM regime. Further analysis of the conduction reveals that the shocked krypton has reached the metallic fluid state due to the high temperature. Besides, the comparisons between the geotherm of deep Earth and the shock states show

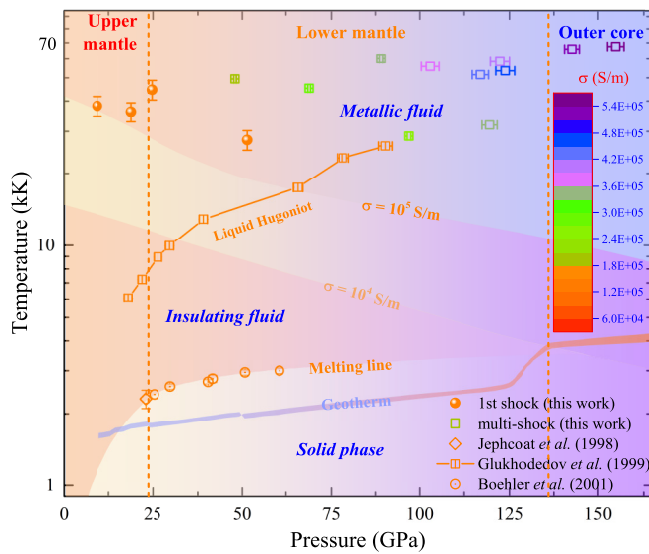


FIG. 4. The distribution of our shock states in the  $T$ - $P$  phase diagram. The first-shock temperatures were determined experimentally (solid ball) and the second- to fourth-shock temperatures (square) were estimated with the SFVT model. The conductivities were obtained from the DFT calculations, and the values are indicated by the color bar. The solid-fluid phase boundaries were derived from the melting curve of solid krypton [5,20] using the laser heated diamond-anvil cell method. The predicted lower ( $10^4$  S/m) and upper ( $10^5$  S/m) insulator-metallic fluid boundaries are taken from Ref. [25]. The Hugoniot of liquid krypton [21] and the mantle geotherm of Earth's interior [5,60] are also shown for comparison.

that our experimental pressure has reached the zone of Earth's outer core. However, there is insufficient information to constrain the state of krypton along the mantle geotherm due to the fact that our shock temperature is far beyond the range of the geotherm. This will be the direction for our follow-up efforts.

#### IV. CONCLUSION

The EOS of dense krypton has been determined up to 155 GPa and 45000 K via multiple-shock reverberation compression experiments. This work fills partially the research void in pressure between high-explosive shock experiments and Z machine experiments and allows for high fidelity comparison with the present DFT theories and chemical models in the WDM regime. Examination of the EOS reveals that the consideration of both the kinetic energy density and the intermediate-range vdW contributions to the fluid krypton is required over a wide  $\rho$ - $P$  region, compared with the conventional PBE and vdW-DF1 XC functionals. The long-range vdW interactions in the SCAN formwork should be treated with caution. The evaluation of the KSDT functional shows that the XC thermal effect will dominate at high temperatures, softening the off-Hugoniot of the dense krypton and improving the agreement with the experimental data. The discussion of the incompleteness of the KSDT functional at lower  $\rho$ - $P$  condition is beyond the scope of this work and it will call for follow-up relevant studies. Finally, combining our data with the previous results, a phase diagram of krypton is given, which may be helpful for understanding the thermophysical behavior of krypton at higher  $T$ - $P$  condition.

#### ACKNOWLEDGMENTS

We thank our colleagues for their assistance with the gas-gun operation, experimental diagnosis, and devices. We are grateful to the anonymous referees for their valuable comments, which are partly included in this work. This work is supported by the Foundation of Laboratory of Shock Wave and Detonation Physics of the China Academy of Engineering Physics (Grant No. JCKYS2018212001), the National Natural Science Foundation of China (Grants No. 11674292, No. 11872057, and No. 12074274), the Science Challenge Project (Grant No. TZ2016001), and the NSAF (Grant No. U1830101). This work is also supported by the TianHe-2 in the LvLiang Cloud Computing Center of China.

- [1] R. Betti and O. A. Hurricane, *Nat. Phys.* **12**, 435 (2016).
- [2] T. Guillot, *Science* **286**, 72 (1999).
- [3] S. Shcheka and H. Keppeler, *Nature (London)* **490**, 531 (2012).
- [4] B. A. Remington, R. P. Drake, and D. D. Ryutov, *Rev. Mod. Phys.* **78**, 755 (2006).
- [5] A. P. Jephcoat, *Nature (London)* **393**, 355 (1998).
- [6] H. F. Wilson and B. Militzer, *Phys. Rev. Lett.* **104**, 121101 (2010).
- [7] P. M. Celliers, P. Loubeyre, J. H. Eggert, S. Brygoo, R. S. McWilliams, D. G. Hicks, T. R. Boehly, R. Jeanloz, and G. W. Collins, *Phys. Rev. Lett.* **104**, 184503 (2010).
- [8] S. Root, R. J. Magyar, J. H. Carpenter, D. L. Hanson, and T. R. Mattsson, *Phys. Rev. Lett.* **105**, 085501 (2010).
- [9] J. H. Carpenter, S. Root, K. R. Cochrane, D. G. Flicker, and T. R. Mattsson, Equation of state of argon: experiments on Z, density functional theory (DFT) simulations, and wide range model, Sandia Report 7791.1 (2012), pp. 1–56.
- [10] J. Zheng, Q. F. Chen, Y. J. Gu, Z. Y. Chen, and C. J. Li, *J. Chem. Phys.* **141**, 124201 (2014).
- [11] R. S. McWilliams, D. A. Dalton, Z. Konopkova, M. F. Mahmood, and A. F. Goncharov, *Proc. Nat. Acad. Sci. USA* **112**, 7925 (2015).
- [12] J. Tang, Y. J. Gu, Q. F. Chen, Z. G. Li, J. Zheng, C. J. Li, and J. T. Li, *Phys. Rev. B* **97**, 140101(R) (2018).
- [13] H. Shimizu, M. Kawajiri, T. Kume, S. Sasaki, Y. A. Freiman, and S. M. Tretyak, *Phys. Rev. B* **79**, 132101 (2009).
- [14] J. Y. Chen, C. S. Yoo, W. J. Evans, H. P. Liermann, H. Cynn, M. Kim, and Z. Jenei, *Phys. Rev. B* **90**, 144104 (2014).
- [15] A. D. Rosa, G. Garbarino, R. Briggs, V. Svitlyk, G. Morard, M. A. Bouhifd, J. Jacobs, T. Irifune, O. Mathon, and S. Pascarelli, *Phys. Rev. B* **97**, 094115 (2018).
- [16] A. Polian, J. M. Besson, M. Grimsditch, and W. A. Grosshans, *Phys. Rev. B* **39**, 1332 (1989).
- [17] A. Polian, J. P. Itie, E. Dartyge, A. Fontaine, and G. Tourillon, *Phys. Rev. B* **39**, 3369 (1989).

- [18] D. Errandonea, B. Schwager, R. Boehler, and M. Ross, *Phys. Rev. B* **65**, 214110 (2002).
- [19] C. Crèpisson, C. Sanloup, L. Cormier, M. Blanchard, J. Hudspeth, A. D. Rosa, O. Mathon, and T. Irifune, *Chem. Geol.* **493**, 525 (2018).
- [20] R. Boehler, M. Ross, P. Söderlind, and D. B. Boercker, *Phys. Rev. Lett.* **86**, 5731 (2001).
- [21] V. D. Glukhodedov, S. I. Kirshanov, T. S. Lebedeva, and M. A. Mochalov, *J. Exp. Theor. Phys.* **89**, 292 (1999).
- [22] T. R. Mattsson, S. Root, A. E. Mattsson, L. Shulenburg, R. J. Magyar, and D. G. Flicker, *Phys. Rev. B* **90**, 184105 (2014).
- [23] S. D. Loch, M. S. Pindzola, C. P. Ballance, D. C. Griffin, D. M. Mitnik, N. R. Badnell, M. G. O'Mullane, H. P. Summers, and A. D. Whiteford, *Phys. Rev. A* **66**, 052708 (2002).
- [24] A. D. Rosa, M. A. Bouhifd, G. Morard, R. Briggs, G. Garbarino, T. Irifune, O. Mathon, and S. Pascarelli, *Earth Planet. Sci. Lett.* **532**, 116032 (2020).
- [25] Z. Q. Wang, Z. G. Li, Y. F. Wang, L. Liu, Y. J. Gu, Q. F. Chen, and X. R. Chen, *Phys. Rev. E* **100**, 033214 (2019).
- [26] M. Schöttler and R. Redmer, *Phys. Rev. Lett.* **120**, 115703 (2018).
- [27] Z. Q. Wang, J. Tang, Y. Hou, Q. F. Chen, X. R. Chen, J. Y. Dai, X. J. Meng, Y. J. Gu, L. Liu, G. J. Li, Y. S. Lan, and Z. G. Li, *Phys. Rev. E* **101**, 023302 (2020).
- [28] H. Sun, D. Kang, J. Dai, W. Ma, L. Zhou, and J. Zeng, *J. Chem. Phys.* **144**, 124503 (2016).
- [29] J. Sun, A. Ruzsinszky, and J. P. Perdew, *Phys. Rev. Lett.* **115**, 036402 (2015).
- [30] J. Sun, R. C. Remsing, Y. Zhang, Z. Sun, A. Ruzsinszky, H. Peng, Z. Yang, A. Paul, U. Waghmare, X. Wu, M. L. Klein, and J. P. Perdew, *Nat. Chem.* **8**, 831 (2016).
- [31] V. V. Karasiev, T. Sjostrom, J. Dufty, and S. B. Trickey, *Phys. Rev. Lett.* **112**, 076403 (2014).
- [32] V. V. Karasiev, L. Calderín, and S. B. Trickey, *Phys. Rev. E* **93**, 063207 (2016).
- [33] V. V. Karasiev, S. X. Hu, M. Zaghoo, and T. R. Boehly, *Phys. Rev. B* **99**, 214110 (2019).
- [34] See Supplemental Material at <http://link.aps.org/supplemental/10.1103/PhysRevB.103.014109> which includes Refs. [11,21,25,29,31–33,37,40–42,46,48–56,58,59], for data analysis, computational method, the summary of the experimental data, and supplemental Figs. S1-S13 and Tables S1-S5.
- [35] M. D. Knudson and M. P. Desjarlais, *Phys. Rev. Lett.* **118**, 035501 (2017).
- [36] J. Wiktor, F. Ambrosio, and A. Pasquarello, *J. Chem. Phys.* **147**, 216101 (2017).
- [37] Q. F. Chen, J. Zheng, Y. J. Gu, and Z. G. Li, *Phys. Plasmas* **22**, 122706 (2015).
- [38] S. P. Lyon and J. D. Johnson, SESAME: The Los Alamos National Laboratory Equation of State Database, LANL Report No. LA-UR-92-3407 (1992).
- [39] W. J. Nellis, *Ultracondensed Matter by Dynamic Compression* (Cambridge University Press, Cambridge, 2017).
- [40] J. Weng, T. Tao, S. Liu, H. Ma, X. Wang, C. Liu, and H. Tan, *Rev. Sci. Instrum.* **84**, 113103 (2013).
- [41] M. D. Knudson, M. P. Desjarlais, R. W. Lemke, T. R. Mattsson, M. French, N. Nettelmann, and R. Redmer, *Phys. Rev. Lett.* **108**, 091102 (2012).
- [42] M. Millot, F. Coppari, J. R. Rygg, A. Correa Barrios, S. Hamel, D. C. Swift, and J. H. Eggert, *Nature (London)* **569**, 251 (2019).
- [43] Z. G. Li, Q. F. Chen, Y. J. Gu, J. Zheng, W. Zhang, L. Liu, G. J. Li, Z. Q. Wang, and J. Y. Dai, *Phys. Rev. B* **98**, 064101 (2018).
- [44] L. Liu, Q. F. Chen, Y. J. Gu, W. Zhang, Z. G. Li, C. J. Li, Z. Q. Wang, G. J. Li, Y. S. Lan, and X. R. Chen, *Appl. Phys. Lett.* **115**, 231905 (2019).
- [45] R. E. Setchell, *J. Appl. Phys.* **50**, 8186 (1979).
- [46] T. S. Duffy and T. J. Ahrens, *J. Appl. Phys.* **82**, 4259 (1997).
- [47] Z. G. Li, Q. F. Chen, Y. J. Gu, J. Zheng, and X. R. Chen, *AIP Adv.* **6**, 105309 (2016).
- [48] N. D. Mermin, *Phys. Rev.* **137**, A1441 (1965).
- [49] A. Baldereschi, *Phys. Rev. B* **7**, 5212 (1973).
- [50] S. Nosè, *J. Chem. Phys.* **81**, 511 (1984).
- [51] J. P. Perdew, K. Burke, and M. Ernzerhof, *Phys. Rev. Lett.* **77**, 3865 (1996).
- [52] M. Dion, H. Rydberg, E. Schröder, D. C. Langreth, and B. I. Lundqvist, *Phys. Rev. Lett.* **92**, 246401 (2004).
- [53] H. Peng, Z.-H. Yang, J. P. Perdew, and J. Sun, *Phys. Rev. X* **6**, 041005 (2016).
- [54] G. Kresse and J. Furthmüller, *Phys. Rev. B* **54**, 11169 (1996).
- [55] V. V. Karasiev, T. Sjostrom, and S. B. Trickey, *Comput. Phys. Commun.* **185**, 3240 (2014).
- [56] M. Chen, J. Xia, C. Huang, J. M. Dieterich, L. Hung, I. Shin, and E. A. Carter, *Comput. Phys. Commun.* **190**, 228 (2015).
- [57] E. W. Brown, B. K. Clark, J. L. DuBois, and D. M. Ceperley, *Phys. Rev. Lett.* **110**, 146405 (2013).
- [58] N. V. Smith, *Phys. Rev. B* **64**, 155106 (2001).
- [59] R. S. McWilliams, D. A. Dalton, M. F. Mahmood, and A. F. Goncharov, *Phys. Rev. Lett.* **116**, 255501 (2016).
- [60] S. Anzellini, A. Dewaele, M. Mezouar, P. Loubeyre, and G. Morard, *Science* **340**, 464 (2013).
- [61] B. Sharpee, Y. Zhang, R. Williams, E. Pellegrini, K. Cavagnolo, J. A. Baldwin, M. Phillips, and X. Liu, *Astrophys. J.* **659**, 1265 (2007).